Beyond Classical Nucleation: Density-Controlled Relaxation Mechanism in Intrinsically Disordered Proteins

Yue Shan(单月)[a], Pengfei Zhang(张朋飞)[b], Chun-Lai Ren(任春来)[a,c,*] and Yu-Qiang Ma(马余强) [a,c,*]

[a] *National Laboratory of Solid State Microstructures and Department of Physics, Collaborative Innovation Center of Advanced Microstructures, Nanjing University, Nanjing 210093, China*
[b] *State Key Laboratory of Advanced Fiber Materials, Center for Advanced Low-Dimension Materials, College of Materials Science and Engineering, Donghua University, Shanghai 201620, China*
[c] *Hefei National Laboratory, Hefei 230088, China*

(Received xxx; accepted manuscript online xxx)

A recent experiment [1] revealed a density transition during nucleation of intrinsically disordered proteins (IDPs), yet its physical origin remains unresolved. Here, using minimal coarse-grained sticker–spacer models, we identify a density-controlled relaxation mechanism governing nucleation under weak multivalent interactions. This mechanism emerges across three hierarchical levels. At the cluster level, nucleation proceeds via reversible, density-regulated nuclei beyond classical nucleation theory. At the molecular level, the configurational distributions of chains within nucleating clusters evolve non-monotonically with cluster size relative to those of isolated single chains, while their conformational fluctuations exhibit exponential relaxation with a characteristic timescale (τ^*). At the bond level, reversible bond turnover accelerates with cluster growth, yielding a characteristic aggregation number (N^*) that marks density saturation and the onset of irreversible growth. The correspondence between τ^* and N^* reveals that nucleation is intrinsically governed by relaxation dynamics. These results establish density-controlled bond turnover as a key kinetic regulator of IDP nucleation and provide a general framework for phase transitions driven by weak multivalent interactions.

Keywords: Intrinsically Disordered Proteins, Nucleation, Coarse-Grained Simulations
DOI: xxxx/xxxx/xx/x/xxxxxx

Introduction. Phase separation driven by weak multivalent interactions underlies the spatiotemporal organization of membraneless organelles in living cells [2–5]. These interactions give rise to dynamic biomolecular condensates whose structure and function are regulated through reversible, specific bonding [6–10]. A hallmark of such condensates is their dynamic nature, characterized by continuous molecular exchange with the surrounding environment [11–14] and rapid internal rearrangements within the dense phase [15,16]. While extensive efforts have connected microscopic interaction rules to equilibrium phase behavior [17–20], how these interactions collectively govern condensate stability and dynamic reorganization remains incompletely understood. Consequently, increasing attention has turned to the dynamics of phase separation in biomolecular systems.

Recent experiments have revealed pronounced nonclassical, multistep nucleation behavior in protein solutions [21–23]. In contrast to classical nucleation theory, protein systems frequently exhibit heterogeneous clusters and transient clusters prior to macroscopic phase separation, even under subsaturated conditions [22–24]. These assemblies act as dynamic solute clusters and liquid precursors, exhibiting large concentration fluctuations and continuously rearranging inner networks [25,26]. Notably, Li et al. [1] recently reported a density transition during nucleation in intrinsically disordered proteins, highlighting progressive densification of nascent clusters. This raises a central question: what are the mechanistic origins of density evolution and reversible cluster formation?

These nonclassical nucleation behaviors are inherently rooted in microscopic interactions, yet unravelling this relationship poses a multiscale challenge. Computational modeling provides a powerful route to address this question. Given the large temporal and spatial scales involved, coarse-grained simulations are particularly well suited. For example, the sticker-and-spacer framework demonstrated a strong coupling between percolation and phase separation mediated by molecular bonding [27–29], while other studies emphasized that role of reversible bonds in determining condensate dynamics [30–33]. However, a direct link between bond dynamics and nucleation behavior is still lacking.

*Corresponding authors. Email: chunlair@nju.edu.cn; myqiang@nju.edu.cn
© 2026 Chinese Physical Society and IOP Publishing Ltd

To bridge this gap and to uncover the multiscale mechanisms underlying nonclassical nucleation, we build on our previous studies of the thermodynamics and dynamics of weak multivalent systems [20,26] and perform Langevin dynamics simulations using a validated minimal sticker–spacer model. This approach enables us to simultaneously resolve nucleation dynamics at three coupled levels, namely cluster growth and densification, single-chain conformational fluctuations, and reversible bond formation and breakage, and to identify the key mechanism that connects them.

Results and Discussion.

Reversible Clusters and Density Transition in IDPs. To quantitatively distinguish the behaviors of classical and nonclassical nucleations, we compare two model systems: homopolymer and intrinsically disordered protein (IDP) solutions, both represented as linear chains of 50 monomers in implicit solvent. In the homopolymer case, all monomers are identical and interact via an attractive Lennard-Jones potential. For the IDP system, we adopt a sticker–and-spacer model originally developed for associative polymer [34,35] to capture weak multivalent interactions. Taking the Fused in Sarcoma (FUS) protein as a representative example, we introduce two types of stickers (T and A) distributed across two blocks of the chain, corresponding to tyrosine residues in the prion-like domain and arginine residues in the RNA-binding domain of FUS, respectively. Each chain contains three T stickers and three A stickers, while all remaining monomers act as spacers. Reversible bonding between T and A stickers gives rise to both intramolecular and intermolecular associations, which have been identified as key drivers of phase separation [20]. Simulations are performed using Langevin dynamics, a method previously validated to reproduce the thermodynamics and dynamics of IDP condensate formation [19,36,37]. Additional details of the coarse-grained model are provided in Materials and Methods.

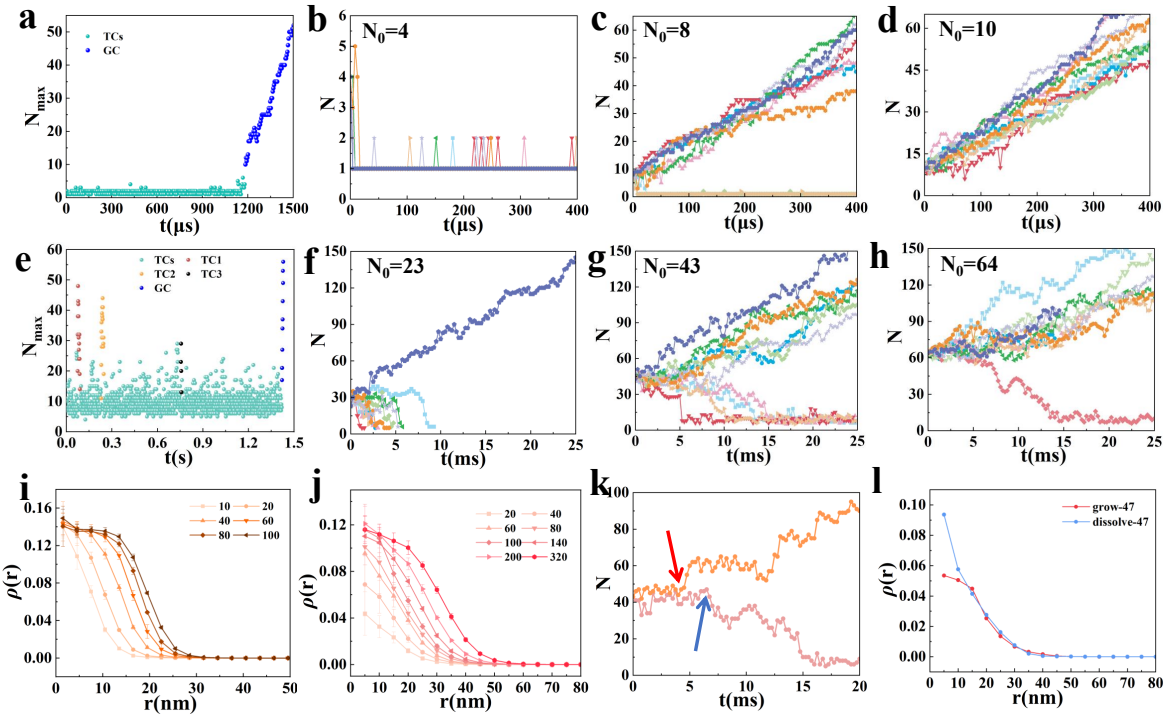

Fig. 1. Early-stage nucleation dynamics. (a)-(d) Homopolymer systems. (a) Time evolution of the largest cluster, quantified by the maximum aggregation number (N_{max}). (b)-(d) Representative trajectories of clusters growth and dissolution for clusters initialized with aggregation numbers $N_0 = 4$, 8 and 10, respectively. (e)-(h) Biopolymer systems. (e) Time evolution of the maximum aggregation number (N_{max}). The abbreviations TCs and GCs are used to represent transient clusters and growing clusters, respectively. TC1, TC2, and TC3 correspond to three distinct transient clusters, respectively. To determine whether the largest cluster at consecutive time steps corresponds to the same evolving cluster, we use the following criterion: we compare the overlap of constituent chains between the two time points. If more than 50% of the chains in the cluster at the earlier time are also present in the cluster at the later time, we consider them to represent the same evolving cluster. (f)-(h) Representative trajectories of clusters initialized with $N_0 = 23$, 43 and 64, respectively (10 trajectories each). (i)-(j) Averaged density profiles as a function of aggregation number for homopolymer (i) and IDP (j) clusters. (k) Two typical trajectories of a cluster with initial size $N_0 = 43$; the arrows indicate two distinct states that both correspond to the same aggregation number $N = 47$. (l) Density profiles corresponding to the two states shown in (k).

To determine the saturation concentration, we performed systematic titration simulations by progressively increasing the protein concentration. Long-timescale Langevin dynamics simulations (exceeding

1.5 seconds) were conducted, and the resulting structure factor $S(q)$ was computed (Fig. S1). Upon phase separation, $S(q)$ exhibits a pronounced increase at low q, indicating the emergence of large-scale protein clustering. From this analysis, we estimated the saturation concentrations to be approximately $c_{sat} \sim 2.33\ \mu M$ for the homopolymer system and $c_{sat} \sim 12.60\ \mu M$ for the IDP system. Accordingly, we selected two supersaturated concentrations: $2.37\ \mu M$ for the homopolymer solution and $12.80\ \mu M$ for the IDP case, corresponding to similar relative supersaturations (c/c_{sat}), to investigate and compare their nucleation behaviors.

The early stages of nucleation involve the emergence of a cluster from the incubation period and its subsequent evolution. To monitor this process, we track the number of chains in the largest cluster, defined as the aggregation number $N_{\max}$, over time. Figure 1 compares the early-stage nucleation dynamics between the homopolymer and IDP systems. In the homopolymer case (Figs. 1a–d), the largest cluster mainly remains as a dimer throughout the incubation period and undergoes a discontinuous growth event at the onset of nucleation. To characterize this change, we select clusters with initial aggregation numbers $N_0 = 4$, 8, and 10, and perform ten independent trajectories for each case. Independent simulations with the same N_0 were started from an identical initial configuration, with both the cluster structure and the spatial distribution of the surrounding chains kept unchanged; only the random seeds for the Langevin dynamics were varied. The clusters with $N_0 = 4$ are consistently unstable and dissolve very quickly on the microsecond timescale, whereas those with $N_0 = 10$ exhibit deterministic growth in all runs. The intermediate case, $N_0 = 8$, displays bistable behavior, with some trajectories growing and others dissolving, indicating its proximity to the critical nucleus. These behaviors align with classical nucleation picture, in which a well-defined critical nucleus of size $\sim N_{critical} = 8$ marks the transition between dissolution and irreversible growth.

For the IDP system (Figs. 1e–h), we observe the emergence of a finite population of transient clusters (TCs) during the incubation regime (Fig. 1e). These clusters have finite lifetimes on the millisecond timescale (Fig. S2a), in accordance with previous reports [21], and their size distribution exhibits a pronounced long tail (Fig. S2b), consistent with earlier observations [22,38]. In contrast to the homopolymer case, where small oligomers ($N \leq 6$ in Fig. S2c) are rarely observed and persist only on the microsecond timescale within the incubation region, a growing cluster ($N > 8$) emerges abruptly from this sparse population of short-lived oligomers, consistent with the classical picture of homogeneous nucleation. In the IDP case, a growing cluster instead emerges continuously from a broad population of long-lived TCs. Notably, both TCs and GCs are highly dynamic, undergoing continuous molecular exchange with their surroundings via two modes: single-molecule exchange or cluster-cluster exchange (Fig. S3). For TCs, analysis of the net change in aggregation number over their lifetimes shows that dissolution can occur through either single-molecule departure or the detachment of subclusters (Fig. S3b). However, the growth of GCs involves cluster fusion events (Fig. S3c), consistent with previous findings [22]. To further investigate the continuous growth behavior of GCs, we perform ten independent trajectories for clusters initialized with $N_0 = 23$, 43, and 64 (Figs. 1f–h). At $N_0 = 23$, dissolution is the dominant outcome, while growth events are rare. At $N_0 = 43$, growth and dissolution occur with comparable probability. At $N_0 = 64$, most clusters grow persistently, and dissolution becomes infrequent. This defines a regime in which clusters are metastable, with competing probabilities of growth and dissolution. We term this the reversible cluster regime, which typically occurs for cluster aggregation number $N > 20$ (Fig. S4) and has recently been observed experimentally [1].

We next examine the internal structure of growing clusters. For homopolymers, averaged radial density profiles computed at various stages of growth reveal that the density distribution is essentially fully developed by the time the cluster reaches $N = 10$ (Fig. 1i). Subsequent increase in aggregation number primarily results in an expansion of cluster size, while the internal density remains approximately unchanged. This behavior indicates the formation of a compact cluster with a well-defined internal structure [39,40]. For IDPs, the situation is markedly different (Fig. 1j). For $N < 100$, density profiles increase continuously with growth and remain broad and diffuse, lacking a sharp boundary with the dilute phase. This observation indicates a density transition in IDPs, accompanied by the emergence of reversible clusters [1]. For $N > 100$, density profiles begin to saturate, giving rise to an inner core and an interface structure. The key distinction between the two models lies in their interaction mode [22]. The homopolymer has a single isotropic interaction scale, favoring the formation of compact clusters with an approximately uniform density. In contrast, the IDP contains distinct interaction scales associated with stickers and spacers, allowing association and structural densification to evolve differently during cluster growth.

As evident from the density profiles, reversible clusters in IDPs exhibit internal heterogeneity. This raises the question: within the density transition regime, how does such nuclear heterogeneity influence subsequent evolution? In Fig. 1k, taking $N_0 = 43$ as an example, we show two typical evolutionary trajectories. One leads to cluster growth and the other results in cluster dissolution. Along these two paths, we selected two states with the same aggregation number ($N = 47$) and marked them with arrows. Fig. 1l displays the density profiles of these two states. Notably, the nucleus destined for dissolution exhibits stronger internal heterogeneity than the one that eventually grows. To quantify this heterogeneity, we calculated the probability distributions of normalized betweenness centrality for the two states, which are constructed from the node-wise normalized betweenness centrality within each individual cluster network. Betweenness centrality reflects the extent to which individual chains participate in the internal connectivity network of the nucleus. The two distributions show different shapes (Fig. S5), with the dissolving nucleus exhibiting a more uneven population of chains across different connectivity levels and a broader distribution. This feature has also been observed in other reversible nuclei in our simulations. Therefore, these results suggest that while the density transition is accompanied by the emergence of heterogeneous structures, excessive heterogeneity appears to disfavor further cluster growth.

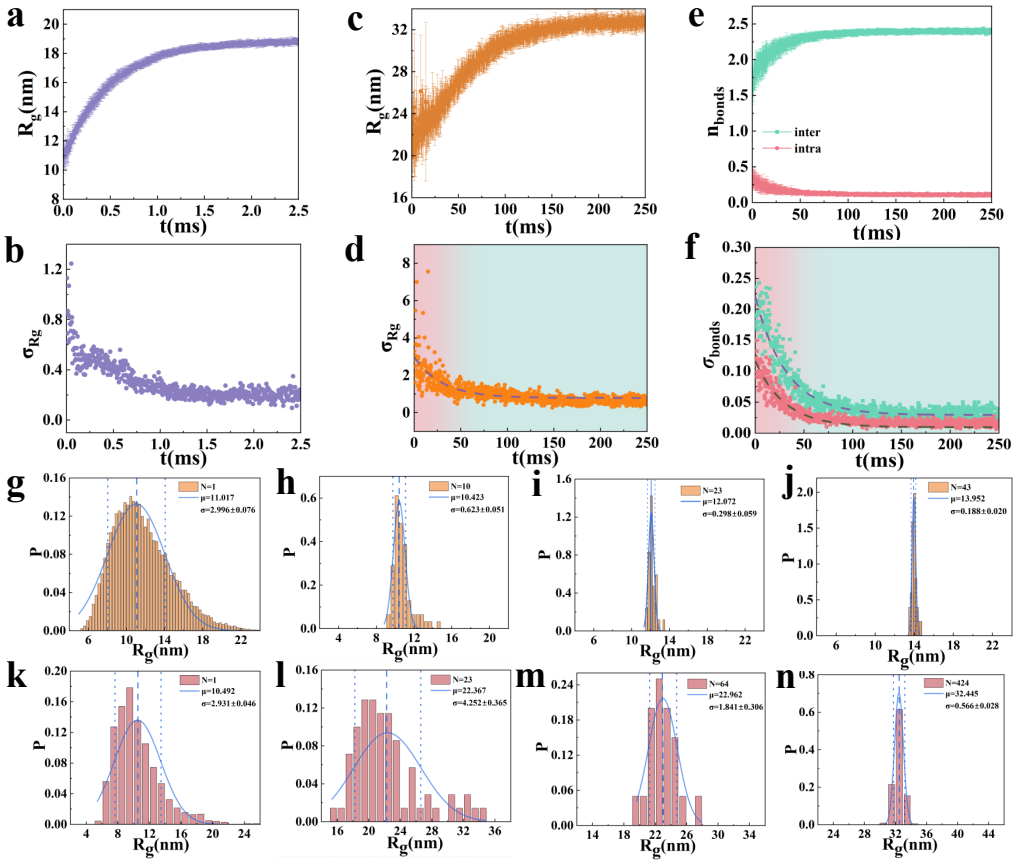

Fig. 2. Chain conformational dynamics. (a-b) Homopolymer systems. (a) Time evolution of the radius of gyration R_g and (b) its standard deviation, quantifying conformational fluctuations. (c-d) Corresponding results for IDP systems. (e) Average numbers of intermolecular and intramolecular bonds per molecule, and (f) their standard deviations for IDPs. (g-j) Probability distributions of R_g for homopolymers and (k-n) for IDPs, each computed from more than 40 conformations. Solid blue curves denote Gaussian fits to the distributions. Blue dashed lines indicate the fitted mean (μ), and blue dotted lines denote $\mu - \sigma$ and $\mu + \sigma$, where σ is the fitted fluctuation width.

Fluctuation Relaxation during IDP Nucleation. To identify the molecular mechanism governing cluster stability, we analyzed the time evolution of the radius of gyration R_g during cluster growth. In the homopolymer system (Fig. 2a), R_g increases gradually with time, reflecting chain extension upon aggregation. The corresponding standard deviation σ_{R_g} (Fig. 2b) decreases rapidly and reaches a plateau, indicating a suppression of conformational fluctuations with increasing aggregation number. The nucleation dynamics of the IDP system (Figs. 2c-d) are substantially slower than those of the homopolymer, with the characteristic nucleation timescale increasing by approximately two orders of magnitude. The mean R_g is nearly twice that of the homopolymer, while the conformational fluctuations σ_{R_g} are approx-

imately one order of magnitude larger. These pronounced and long-lived conformational fluctuations indicate that chain conformational fluctuation relaxation cannot be neglected relative to cluster growth. We therefore treat the slow conformational evolution of the IDP system as a relaxation process by fitting $\sigma_{R_g}(t)$ to an exponential relaxation (Fig. 2d): $\frac{d(\sigma_{R_g}-\sigma_{equ})}{dt} = -\frac{1}{\tau^*}(\sigma_{R_g}-\sigma_{equ})$. Here, σ_{equ} is the standard deviation of R_g in the equilibrium condensate and τ^* is the characteristic relaxation time. The fit yields $\tau^* = 30.20 \pm 2.59\ ms$.

Notably, earlier studies [18] have reported that R_g of IDP molecules inside condensates (the dense phase) is distinctively larger than that in the dilute phase. This difference has been attributed to the need for IDP molecules in the dilute phase to break intramolecular bonds and form intermolecular bonds to drive condensation. Our simulations reproduce this trend (Fig. S6), which readily explains why the increase in R_g is far more pronounced in IDPs than in homopolymers. But why does σ_{R_g} decay slowly and exponentially with time? In Fig. 2e-f, we find that the fluctuations in the numbers of intramolecular and intermolecular bonds, quantified by σ_{bonds}, exhibit a similar exponential decay. Specifically, the characteristic relaxation times are $\tau^* = 31.60 \pm 1.06\ ms$ and $30.31 \pm 3.27\ ms$ for the fluctuations of intermolecular and intramolecular bonds, respectively. Both values are in good agreement with that obtained from the σ_{R_g} analysis. Although the mean R_g and bond number exhibit distinct temporal evolution due to the combined effects of sticker-mediated bonding and molecular crowding, their fluctuations share a consistent characteristic relaxation timescale, suggesting that both observables are governed by a common underlying relaxation process. This correspondence reveals that the molecular origin of the relaxation lies in the conformational rearrangement driven by the intramolecular-to-intermolecular bond conversion during early-stage nucleation.

To further understand this fluctuation relaxation, we compare the R_g distributions at different aggregation numbers. For each cluster size, the R_g distribution was constructed by pooling all corresponding configurations sampled from 20 independently initialized simulation trajectories, with sampling intervals chosen sufficiently long to reduce temporal correlations between successive configurations. In the homopolymer system (Figs. 2g-j), the conformational space progressively narrows with cluster growth, reflecting enhanced confinement of free chains. For IDPs (Figs. 2k-n), the width of the R_g distribution varies nonmonotonically with cluster size compared with that of the isolated chain. At $N = 23$, the distribution of R_g broadens significantly relative to the isolated-chain state, indicating that oligomeric aggregation enhances conformational accessibility. At larger N, the distribution narrows again as the increased internal density suppresses fluctuations, with the decay becoming progressively faster at higher densities. This nonmonotonic behavior of molecular configuration from isolated chains to growing clusters shows that conformational fluctuation relaxation in IDPs is not merely a reduction of conformational freedom upon condensation, as observed in homopolymers. Rather, a modest increase in local concentration triggers conformational changes through intramolecular-to-intermolecular bond conversion, which is inherently a collective effect. This density-controlled, fluctuation-enabled exploration provides a dynamic route in which both growth and dissolution remain accessible, offering a physical basis for the reversible clustering in weak multivalent systems.

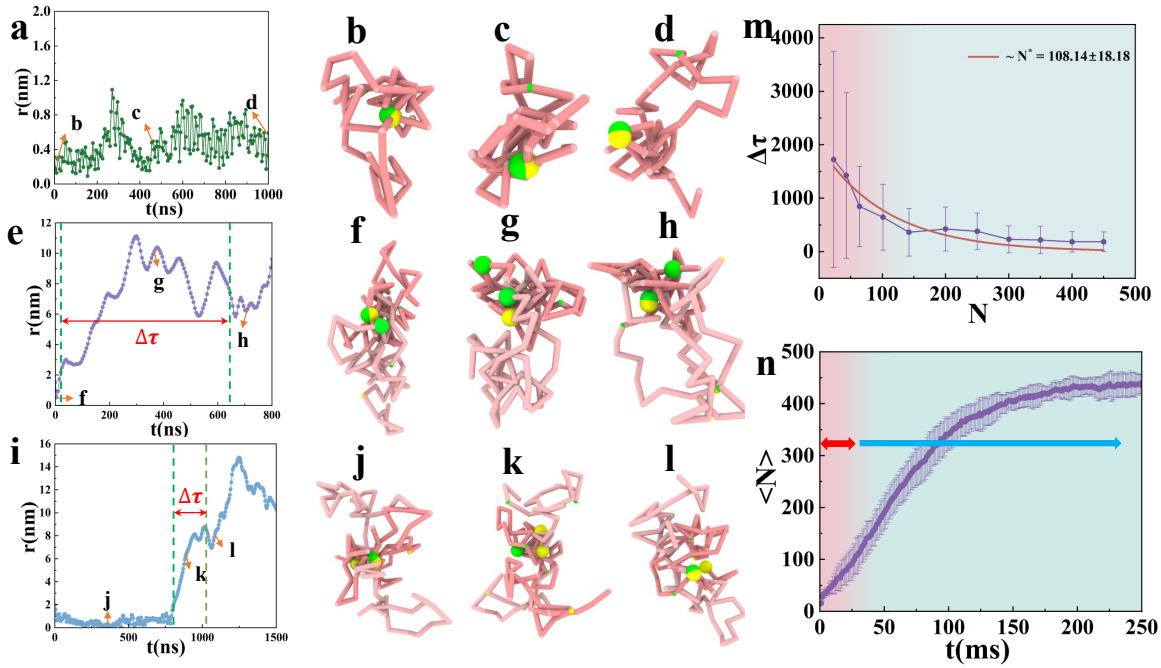

Fig. 3. Bond turnover dynamics in IDPs. Representative cases with aggregation numbers N=1 (a-d), N=64 (e-h), and N=424 (i-l) are shown. Bond-level dynamics are characterized by the temporal evolution of the distance between two stickers (yellow and green) that are initially bonded. A bond is defined by an inter-sticker distance smaller than 2 *nm*. For each case, three representative conformations are shown. (b-d) indicates the intramolecular bond keeping stable within the simulation duration. (f-h) and (j-l) illustrate the intramolecular bond breaking (yellow and green) and intermolecular reformation (yellow-red or green-red) process. $\Delta\tau$ denotes the time interval between bond breaking and subsequent bond formation. (m) The averaged $\Delta\tau$, obtained from 50 independent bond-breaking events for clusters with different aggregation numbers, is shown as a function of aggregation number. (n) Temporal evolution of the average cluster aggregation number. The reversible clusters regime, indicated by the red double-arrow region, is highlighted in the nucleation curve. The blue arrow marks the irreversible growth regime.

Bond Turnover Dynamics in IDPs. Since chain conformational dynamics in IDPs is intrinsically coupled to microscopic bond-breaking and bond-forming events, we next examine bond turnover dynamics to link them to density-controlled relaxation process. To quantify the turnover dynamics, we track pairs of initially bonded stickers by monitoring the distance between their centers of mass. A bond is defined as broken when this distance exceeds 2 nm. Owing to the reversible nature of the interactions, bond dissociation can be followed by reformation of new bonds.

Figures 3a–d show bond evolution within an isolated chain, where no bond breaking is observed within the simulation timescale. However, Figs. 3e–h show a representative bond within a cluster of $N = 64$, in which both dissociation and reformation are observed. We define the time interval between bond dissociation and subsequent reformation as $\Delta\tau$ to characterize the bond turnover events. Figures 3i–l extend this analysis to larger clusters ($N = 424$). Figure 3m shows the average $\Delta\tau$ obtained from 50 independent bond-breaking and rebinding events for different clusters. We find that $\Delta\tau$ decreases exponentially with increasing cluster aggregation number N, indicating progressively faster bond turnover and enhanced kinetic stability in larger clusters. An exponential fit yields a characteristic aggregation number of $N^* = 108.14 \pm 18.81$. As shown in Fig. 3n, the average aggregation number of the cluster increases with time, reaching $< N >= 112.10 \pm 33.88$ at $t = 30$ ms, in good agreement with N^*. Furthermore, the characteristic values obtained from the exponential relaxation of σ_{R_g}, σ_{bonds} and $\Delta\tau$ are summarized in SI Table, indicating that these observables are governed by a common underlying relaxation process. Together, these results indicate that increased density promotes bond turnover, suppresses chain conformational fluctuations and drives the transition from reversible to irreversible clusters. Moreover, bond turnover dynamics offer direct evidence for ultrafast dynamics inside the condensate [15].

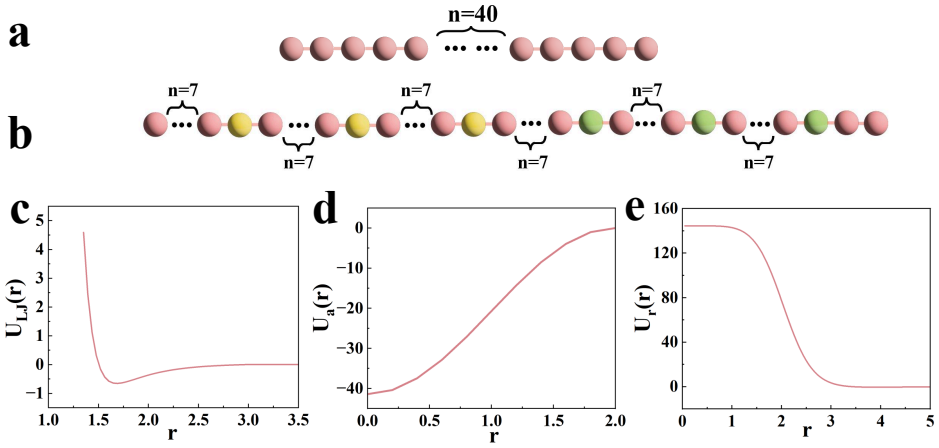

Fig. 4. Coarse-grained models and interaction potentials used to investigate condensate nucleation.(a) Schematic representation of the homopolymer model, in which all beads are identical.(b) Schematic representation of the biopolymer model within the sticker-and-spacer framework. Green and yellow beads denote two complementary sticker types, whereas pink beads represent spacer beads. Each polymer contains alternating sticker and spacer segments that enable multivalent interactions.(c) Lennard–Jones interaction potential used between beads in the homopolymer model.(d) Attractive interaction potential governing specific sticker–sticker binding in the biopolymer model.(e) Repulsive interaction potential applied between spacer–spacer and sticker–spacer pairs to prevent nonspecific aggregation.

Conclusion. In this study, we identify a unified, density-controlled relaxation process that governs nonclassical nucleation in intrinsically disordered proteins (IDPs) driven by weak multivalent interactions. By resolving nucleation at three coupled levels: cluster growth, conformational fluctuations, and bond turnover, we show that IDP nucleation proceeds through a reversible cluster regime, contrasting with the classical pathway defined by a sharp critical nucleus. Our results reveal that conformational fluctuations, bond number variations, and bond turnover dynamics converge onto a single relaxation process, characterized by a timescale $\tau^* \sim 30$ ms and a characteristic aggregation number $N^* \sim 108$. This convergence demonstrates that nucleation is intrinsically coupled to molecular relaxation, where increased density accelerates bond turnover, suppresses conformational fluctuations, and drives the transition from reversible to irreversible clusters. Our results suggest that nucleation in weakly multivalent systems is better viewed as a multidimensional stochastic dynamical process, in which cluster growth is coupled to the relaxation of internal conformational and density fluctuations, rather than as the crossing of a single critical cluster size. This framework goes beyond the conventional one-dimensional, size-based description of classical nucleation, highlighting the essential role of internal relaxation and stochastic fluctuations in determining nucleation fate (Fig. S7).

The biological significance of reversible clusters may extend beyond the nucleation process itself. Weak multivalent interactions are a ubiquitous feature of intrinsically disordered proteins and RNA-binding proteins involved in condensate formation, including FUS [41], hnRNPA1 [42], TDP-43 [43], and numerous signaling scaffolds [44]. Increasing evidence suggests that mesoscale and transient clusters can act as functional intermediates that locally concentrate biomolecules, accelerate biochemical reactions, and enhance the sensitivity of cellular regulatory networks [45–47]. From this perspective, the emergence of reversible clusters may provide a mechanism for achieving local enrichment without committing the system to irreversible condensation [48]. Furthermore, maintaining condensates in a reversible cluster regime may help cells balance functional assembly against pathological aggregation. Functional condensates must remain dynamic enough to exchange components and respond to environmental signals, whereas excessive stabilization can promote gelation, aging, and ultimately amyloid formation [49–51]. The reversible cluster regime identified here occupies an intermediate state between dispersed molecules and stable condensates, allowing condensates to achieve transient organization while avoiding kinetic trapping. Such metastable assemblies may therefore represent an evolutionary strategy for maximizing functional adaptability while minimizing the risk of irreversible aggregation.

Materials and Methods. Schematic representations of the homopolymer model and the sticker-and-spacer biopolymer model are shown in Figs. 4a and 4b, respectively. In both systems, each chain consists of 50 beads connected by harmonic bonds. The distinct interaction potentials governing the two models are shown in Figs. 4c-e, with their functional forms and parameter values detailed in the Supplementary Information (SI).

All simulations were performed using Langevin dynamics in the NVT ensemble with periodic boundary conditions in a cubic box of size $450 \times 450 \times 450$ nm^3. The sticker-and-spacer model was simulated in physical units at 300 K, while the homopolymer model was simulated in reduced Lennard–Jones units and subsequently mapped to physical units. Additional simulation parameters and unit conversion details are provided in SI. All simulations were performed using the LAMMPS molecular dynamics package (version 23 June 2023) [52].

Acknowledgements. We are grateful to the High Performance Computing Center (HPCC) of Nanjing University for performing the numerical calculations in this paper on its blade cluster system. This work is supported by the Fundamental and Interdisciplinary Disciplines Breakthrough Plan of the Ministry of Education of China (Grant No. JYB2025XDXM502), the National Key Research and Development Program of China (Grant No. 2022YFA1405000), the National Natural Science Foundation of China (Grant Nos. 12274212, 12347102 and 12547146), the Natural Science Foundation of Jiangsu Province (Grant No. BK20233001), the Innovation Program for Quantum Science and Technology (Grant No. 2024ZD0300101), and Jiangsu Funding Program for Excellent Postdoctoral Talent (Grant No. 2025ZB391).

Supporting Information. Additional supporting information can be found online in the Supporting Information section.

References

[1] Li J.-Y, Niu Y.-H, Gao Y.-Q, and Wang H 2026 *Natl. Sci. Rev.* **13** nwag107

[2] Brangwynne C. P, Eckmann C. R, Courson D. S, Rybarska A, Hoege C, Gharakhani J, Jülicher F, and Hyman A. A 2009 *Science* **324** 1729

[3] Brangwynne C. P, Mitchison T. J, and Hyman A. A 2011 *Proc. Natl. Acad. Sci. U.S.A.* **108** 4334–4339

[4] Brangwynne C. P, Tompa P, and Pappu R. V 2015 *Nat. Phys.* **11** 899

[5] Dolgin E 2018 *Nature* **555** 300–302

[6] Lee K.-H, Zhang P, Kim H. J, Mitrea D. M, Sarkar M, Freibaum B. D, Cika J, Coughlin M, Messing J, Molliex A, and others 2016 *Cell* **167** 774–788

[7] Alberti S, Gladfelter A, and Mittag T 2019 *Cell* **176** 419–434

[8] Banani S. F, Lee H. O, Hyman A. A, and Rosen M. K 2017 *Nat. Rev. Mol. Cell Biol.* **18** 285–298

[9] Wang J, Choi J.-M, Holehouse A. S, Lee H. O, Zhang X, Jahnel M, Maharana S, Lemaitre R, Pozniakovsky A, Drechsel D, and others 2018 *Cell* **174** 688–699

[10] Li P 2026 *J. Mol. Biol.* **438** 169680

[11] Feric M, Vaidya N, Harmon T. S, Mitrea D. M, Zhu L, Richardson T. M, Kriwacki R. W, Pappu R. V, and Brangwynne C. P 2016 *Cell* **165** 1686–1697

[12] Jawerth L. M, Ijavi M, Ruer M, Saha S, Jahnel M, Hyman A. A, Jülicher F, and Fischer-Friedrich E 2018 *Phys. Rev. Lett.* **121** 258101

[13] Caragine C. M, Haley S. C, and Zidovska A 2018 *Phys. Rev. Lett.* **121** 148101

[14] Gouveia B, Kim Y, Shaevitz J. W, Petry S, Stone H. A, and Brangwynne C. P 2022 *Nature* **609** 255–264

[15] Galvanetto N, Ivanović M. T, Chowdhury A, Sottini A, Nüesch M. F, Nettels D, Best R. B, and Schuler B 2023 *Nature* **619** 876–883

[16] Song H, Cui J, Hu G, Xiong L, Wutthinitikornkit Y, Lei H, and Li J 2025 *Adv. Sci.* **12** 2412989

[17] Lee C. F, Brangwynne C. P, Gharakhani J, Hyman A. A, and Jülicher F 2013 *Phys. Rev. Lett.* **111** 088101

[18] Martin E. W, Holehouse A. S, Peran I, Farag M, Incicco J. J, Bremer A, Grace C. R, Soranno A, Pappu R. V, and Mittag T 2020 *Science* **367** 694–699

[19] Zhang Y, Xu B, Weiner B. G, Meir Y, and Wingreen N. S 2021 *eLife* **10** e62403

[20] Ren C.-L, Shan Y, Zhang P, Ding H.-M, and Ma Y.-Q 2022 *Sci. Adv.* **8** eabo7885

[21] Martin E. W, Harmon T. S, Hopkins J. B, Chakravarthy S, Incicco J. J, Schuck P, Soranno A, and Mittag T 2021 *Nat. Commun.* **12** 4513

[22] Kar M, Dar F, Welsh T. J, Vogel L. T, Kühnemuth R, Majumdar A, Krainer G, Franzmann T. M, Alberti S, Seidel C. A, and others 2022 *Proc. Natl. Acad. Sci. U.S.A.* **119** e2202222119

[23] Lan C, Kim J, Ulferts S, Aprile-Garcia F, Weyrauch S, Anandamurugan A, Grosse R, Sawarkar R, Reinhardt A, and Hugel T 2023 *Nat. Commun.* **14** 4831

[24] Ge Y, Paul T, Gordiychuk M, Das N, Zhang Y, and Myong S 2025 *Nat. Commun.* **16** 9956

[25] Shin Y and Brangwynne C. P 2017 *Science* **357** eaaf4382

[26] Xiang Y.-X, Shan Y, Lei Q.-L, Ren C.-L, and Ma Y.-Q 2022 *Phys. Rev. E* **106** 044403

[27] Farag M, Borcherds W. M, Bremer A, Mittag T, and Pappu R. V 2023 *Nat. Commun.* **14** 5527

[28] Jeong-Mo C, Dar F, and Pappu R. V 2019 *PLoS Comput. Biol.* **15** e1007028

[29] Choi J.-M, Hyman A. A, and Pappu R. V 2020 *Phys. Rev. E* **102** 042403

[30] Dignon G. L, Zheng W, Kim Y. C, Best R. B, and Mittal J 2018 *PLoS Comput. Biol.* **14** e1005941

[31] Regy R. M, Dignon G. L, Zheng W, Kim Y. C, and Mittal J 2020 *Nucleic Acids Res.* **48** 12593–12603

[32] Benayad Z, Bulow S, Stelzl L. S, and Hummer G 2020 *J. Chem. Theory Comput.* **17** 525–537

[33] Joseph J. A, Reinhardt A, Aguirre A, Chew P. Y, Russell K. O, Espinosa J. R, Garaizar A, and Collepardo-Guevara R 2021 *Nat. Comput. Sci.* **1** 732–743

[34] Tanaka F 1989 *Macromolecules* **22** 1988–1994

[35] Semenov A. N and Rubinstein M 1998 *Macromolecules* **31** 1373–1385

[36] Ronceray P, Zhang Y, Liu X, and Wingreen N. S 2022 *Phys. Rev. Lett.* **128** 038102

[37] Ranganathan S and Shakhnovich E. I 2020 *eLife* **9** e56159

[38] Amico T, Dada S. T, Lazzari A, Brezinova M, Trovato A, Vendruscolo M, Fuxreiter M, and Maritan A 2024 *eLife* **13** RP94214

[39] Oxtoby D. W 1992 *J. Phys.: Condens. Matter* **4** 7627–7650

[40] Sear R. P 2007 *J. Phys.: Condens. Matter* **19** 033101

[41] Patel A, Lee H. O, Jawerth L, Maharana S, Jahnel M, Hein M. Y, Stoynov S, Mahamid J, Saha S, Franzmann T. M, and others 2015 *Cell* **162** 1066–1077

[42] Molliex A, Temirov J, Lee J, Coughlin M, Kanagaraj A. P, Kim H. J, Mittag T, and Taylor J. P 2015 *Cell* **163** 123–133

[43] Conicella A. E, Dignon G. L, Zerze G. H, Schmidt H. B, D'Ordine A. M, Kim Y. C, Rohatgi R, Ayala Y. M, Mittal J, and Fawzi N. L 2020 *Proc. Natl. Acad. Sci. U.S.A.* **117** 5883–5894

[44] Li P, Banjade S, Cheng H.-C, Kim S, Chen B, Guo L, Llaguno M, Hollingsworth J. V, King D. S, Banani S. F, and others 2012 *Nature* **483** 336–340

[45] Peeples W and Rosen M. K 2021 *Nat. Chem. Biol.* **17** 693–702

[46] Arter W. E, Qi R, Erkamp N. A, Krainer G, Didi K, Welsh T. J, Acker J, Nixon-Abell J, Qamar S, Guillén-Boixet J, and others 2022 *Nat. Commun.* **13** 7845

[47] Yanas A, Shweta H, Owens M. C, Liu K. F, and Goldman Y. E 2024 *Curr. Biol.* **34** 5714–5727

[48] Zeng X and Pappu R. V 2025 *Commun. Chem.* **8** 106

[49] Shen Y, Ruggeri F. S, Vigolo D, Kamada A, Qamar S, Levin A, Iserman C, Alberti S, George-Hyslop P. S, and Knowles T. P 2020 *Nat. Nanotechnol.* **15** 841–847

[50] Jawerth L, Fischer-Friedrich E, Saha S, Wang J, Franzmann T, Zhang X, Sachweh J, Ruer M, Ijavi M, Saha S, and others 2020 *Science* **370** 1317–1323

[51] Alberti S and Hyman A. A 2021 *Nat. Rev. Mol. Cell Biol.* **22** 196–213

[52] Plimpton S 1995 *J. Comput. Phys.* **117** 1–19